Research Article Vol. 32, No. 17 / 12 Aug 2024 / *Optics Express* 30879

Optics EXPRESS

Fast and efficient hard X-ray projection imaging below 10 nm resolution

WENHUI ZHANG,[1,7] J. LUKAS DRESSELHAUS,[2] HOLGER FLECKENSTEIN,[1] MAURO PRASCIOLU,[1] MARGARITA ZAKHAROVA,[1] NIKOLAY IVANOV,[1] CHUFENG LI,[1] OLEKSANDR YEFANOV,[1] TANG LI,[2] DMITRY EGOROV,[1] IVAN DE GENNARO AQUINO,[1] PHILIPP MIDDENDORF,[1] JOHANNES HAGEMANN,[3] SHAN SHI,[4,5] SAŠA BAJT,[1,2,8] AND HENRY N. CHAPMAN[1,2,6,9]

[1] *Center for Free-Electron Laser Science CFEL, Deutsches Elektronen-Synchrotron DESY, Notkestr. 85, 22607 Hamburg, Germany*
[2] *The Hamburg Centre for Ultrafast Imaging, 22761 Hamburg, Germany*
[3] *Center for X-ray and Nano Science CXNS, Deutsches Elektronen-Synchrotron DESY, Notkestr. 85, 22607 Hamburg, Germany*
[4] *Research Group of Integrated Metallic Nanomaterials Systems, Hamburg University of Technology, 21073 Hamburg, Germany*
[5] *Institute of Hydrogen Technology, Helmholtz-Zentrum Hereon, 21502 Geesthacht, Germany*
[6] *Department of Physics, Universität Hamburg, 22761 Hamburg, Germany*
[7] *wenhui.zhang@desy.de*
[8] *sasa.bajt@desy.de*
[9] *henry.chapman@desy.de*

Abstract: High-resolution X-ray imaging of noncrystalline objects is often achieved through the approach of scanning coherent diffractive imaging known as ptychography. The imaging resolution is usually limited by the scattering properties of the sample, where weak diffraction signals at the highest scattering angles compete with parasitic scattering. Here, we demonstrate that X-ray multilayer Laue lenses with a high numerical aperture (NA) can be used to create a strong reference beam that holographically boosts weak scattering from the sample over a large range of scattering angles, enabling high-resolution imaging that is tolerant of such background. An imaging resolution of sub-10 nm was achieved at a photon energy of 17.4 keV with lenses of 0.014 NA from a Siemens star test object and a sample of hierarchical nanoporous gold, recording projection holograms at an effective magnification of more than 30,000 directly on a pixel-array detector. A numerical study compared this approach to low-NA far-field ptychography, indicating significant advantages for using high-NA lenses in the presence of background noise. This imaging modality is particularly fast and efficient at recording high-resolution transmission phase-contrast images over large fields of view in a facile manner.

1. Introduction

High-resolution characterization of materials is essential for understanding and improving functional and active materials, such as catalysts, solar cells, batteries, storage media, and integrated circuits. Imaging of such materials at the nanoscale is required to understand the relationships between microstructure and various mechanical, electronic, or magnetic properties. The rise in the brightness of synchrotron radiation sources over the last several decades has led to extensive developments [1–8] in X-ray imaging and tomography in the photon energy range of approximately 5 keV to 20 keV to fulfill this need. Given the weak interaction of

#532037 https://doi.org/10.1364/OE.532037
Journal © 2024 Received 4 Jun 2024; revised 26 Jul 2024; accepted 28 Jul 2024; published 9 Aug 2024

X-rays with matter in this spectral range, phase-contrast and diffraction-based imaging methods offer the highest sensitivity for the investigation of nanostructures in bulk samples (thicker than approximately 1 μm). However, for this same reason, efficiently deflecting X-rays by significant angles is difficult, which has limited the creation of high-resolution lenses. To overcome this restriction, the method of ptychography is often used [3]. By measuring diffraction patterns from several localized and overlapping regions of the sample as it is stepped across a focused beam, it is possible to recover the complex-valued exit wave of the sample at a resolution dependent on the angular extent of the measured diffraction rather than the numerical aperture (NA) of the focused X-ray beam (the probe). In this way, a half-period resolution of 5 nm was obtained at a soft X-ray wavelength of 1.7 nm with a probe size of 150 nm (Ref. [9]), and a half-period resolution of 10 nm was achieved at a 0.2 nm wavelength—much better than the information limit of the probe (700 nm in size) [10]. The imaging resolution in these examples was ultimately limited by the strength of the diffraction signal. This is generally the case since the diffraction intensities tend to decrease with increasing resolution length d (Ref. [11]). Improving the resolution requires ever increasing the incident fluence and hence the radiation dose to the sample (which it might not be able to tolerate) [12]. However, it is often not possible to extract the full potential signal for a given dose since the weakest diffraction (at the highest scattering angles) may be dominated by background scattering from air, beamline slits, or the focusing optic itself. Furthermore, diffraction signals usually vary over a dynamic range of many tens of thousands—from single photons to direct beams—often requiring multiple exposures. Thus, the resolution increase achieved in X-ray ptychography, compared to scanning transmission microscopy, usually comes at a higher cost of imaging speed, dose, and radiation damage than ultimately necessary.

With the recent development and use of multilayer Laue lenses (MLLs) [13,14], it has become possible to focus hard X-rays with a high convergence angle (or NA) to give diffraction-limited spot sizes smaller than approximately 4 nm (Ref. [15]). These diffractive lenses are fabricated layer by layer by magnetron sputtering—a process in which errors in layer placement can accumulate, resulting in aberrations that may be several waves in magnitude [15]. Although such errors can be compensated for, for example, by the use of a refractive corrector, [16,17] they do not necessarily restrict the large angular divergence of the probe beam. In a ptychography measurement, this large divergence overcomes the problems of high dynamic range and sensitivity to weak diffraction signals by providing a strong zero-order reference beam that interferes coherently with the scattering from the sample. When placed in the focal plane, the sample needs to be stepped by distances that are even smaller than the probe size to obtain a ptychographic dataset. This leads to datasets with a large number of steps for the scanned object, coupled with modest requirements on the number of pixels required to record the diffraction pattern [18]. A certain field of view can be covered in far fewer steps (and detector frames) by placing the sample considerably out of focus, thus giving a high-speed data acquisition. In this case, the diffraction pattern must be sampled more finely to match the larger width of the probe. However, given that direct-detection pixel array detectors with large pixel numbers are widely available for X-rays, this approach—known as near-field ptychography [19]—may have practical benefits in terms of speed and less demanding requirements for sample scanning hardware.

When a weakly scattering object is placed outside of the focus of a converging beam, a magnified projection image is formed in the far field of that focus, with a magnification $M = L/\Delta f$ equal to the ratio of the distance from the focus to the detector, L, to the defocus distance Δf. It is well known that this projection image is equal to a magnified version of the in-line hologram that would be obtained by illuminating the object with a plane wave, measured at approximately the defocus distances [20–22], as shown schematically in Fig. 1(a). This hologram is equivalent to the defocused coherent image from a transmission X-ray microscope under plane-wave illumination and using an objective of the same NA [23]. In all three cases, the image is equal to the Fresnel transform of the transmission function of the object. For small defoci, the contrast of such images of pure phase objects increases with Δf (Ref. [24]).

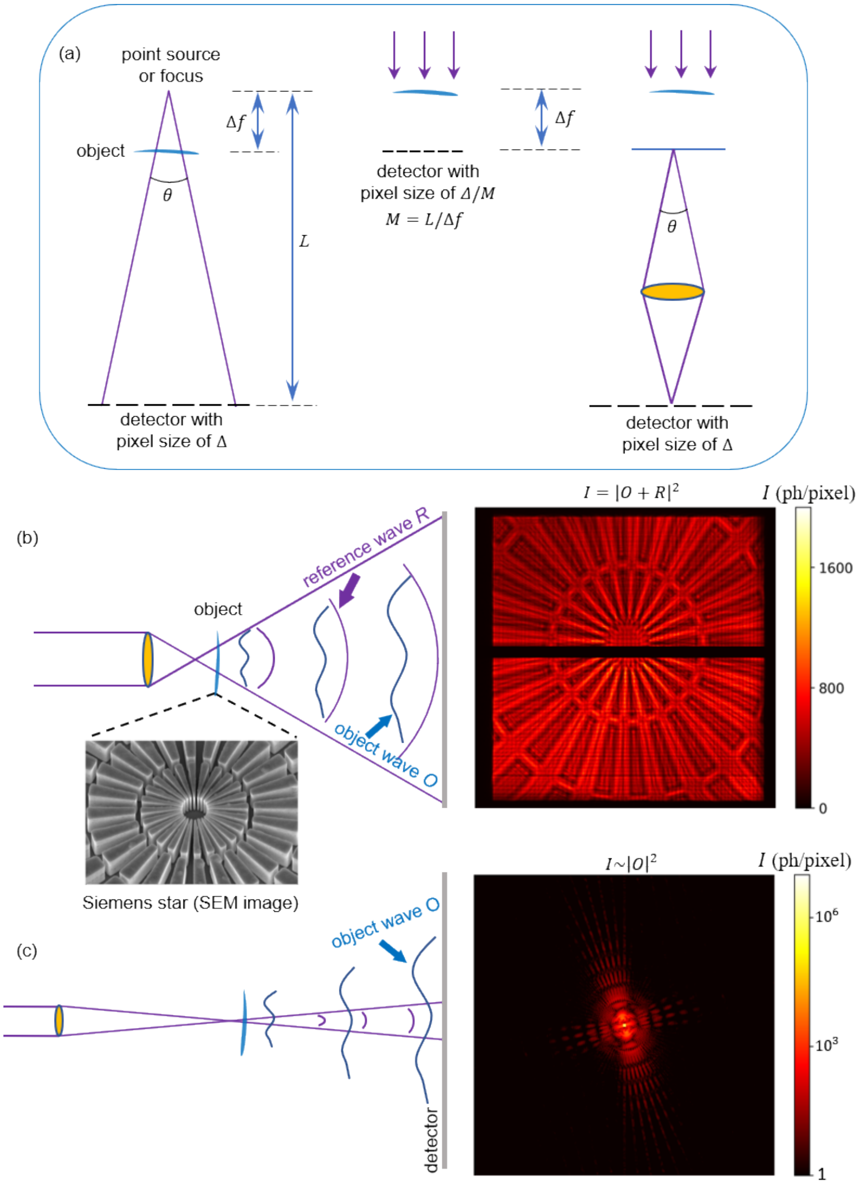

Fig. 1. (a) Equivalence of point projection holography (left), in-line holography (middle), and a defocused microscope image (right). The object wave O in point projection holography (b) is boosted by the reference R and thus can exceed background scattering from air, apertures or optical elements. Far-field diffraction patterns (c) are weak at highest scattering angles and may easily be corrupted by such scattering noise. The point projection hologram in (b) was measured from a Siemens star object (see text) and is displayed on a linear color scale. The diffraction pattern in (c) was simulated and is displayed on a logarithmic color scale. The label ph/pixel stands for the number of photons per pixel.

Returning to the holographic interpretation of the projection image, the reference wave is provided by the beam diverging from the focus and not interacting with the object. Obviously, at the detector, this reference wave R only extends to scattering angles covered by the diverging beam, as given by the NA of the lens. Within this range, the interference between R and the diffraction

O from an object can be considered $|O+R|^2 = |R|^2 + 2|O\,R|\cos\phi + |O|^2$. The relative phase ϕ between the object and reference is encoded in the hologram. In the hard X-ray regime, most (microscopic) objects are weakly scattering such that the reference-beam intensity $|R|^2$ is many thousand times greater than the far-field diffraction signal $|O|^2$, which can therefore be neglected in the region of the reference. The term $2|O\,R|\cos\phi$ shows that the diffraction signal of the object is greatly amplified by the strength of the reference amplitude. For complete constructive or destructive interference ($\phi = 0$ or π), this boost factor is equal to $2|OR|/|O|^2 = 2|R|/|O|$, and the contrast of the hologram is $2|O|/|R|$. Both the non-holographic diffraction signal $|O|^2$ and the boosted holographic signal $2|OR|\cos\phi$ exhibit Poisson noise. When photon counting is the only noise source, the signal-to-noise advantage obtained by including the reference is actually only a factor of $2\cos\phi$, with a root-mean-square value of $\sqrt{2}$.

Although studies have shown that coherent mixing of the signal with a strong reference does not necessarily improve the signal-to-noise ratio of reconstructed images [25], the signal boost and the large offset $|R|^2$ will dominate any extraneous scattering. A recent study on coherent soft X-ray imaging of magnetic structures demonstrated that the addition of a holographic reference wave does improve the achievable image resolution and contrast [26]. Additionally, compared to the diffraction signal $|O|^2$ without a reference, the boosted (low-contrast) holographic signal covers a much lower dynamic range, easing the requirements of the detector, and the in-line hologram generally requires a lower degree of spatial coherence to encode the transmission function than does the far-field pattern [27].

There have been several challenges in realizing high-resolution X-ray imaging in the holographic regime. One has been the production of a strong reference that covers a suitably large range of scattering angles. Objects such as gold particles [28], pinholes [26,29,30], and aerogels [31] have been used or suggested. These tend to provide reference beams that are not much stronger than the scattering from the object and that vary considerably in intensity. A strong reference was created by the focused beam of a soft X-ray zone plate [32], although the usable angular range was restricted by the annular pupil. Another challenge is how best to reconstruct the transmission function of an object (its exit wave) from a hologram and, in particular, how to overcome the twin-image problem for inline geometry. Near-field ptychography [19] using MLLs overcomes both of these challenges, although when framed as a series of holographic images recorded for various shifts of the object relative to the illumination, it is not immediately clear how this approach recovers the object's transmission function. For a perfect (unaberrated) wavefield, stepping the object across the beam at a fixed defocus would simply shift the projected hologram across the illuminated region of the detector without providing new information. For a perfect spherical wave, only changing defocus gives the needed diversity [24,32]. A structured wavefront created by a diffuser enables image reconstruction without changing the focus [19]. The illumination phase at any point r_0 can be approximated through a truncated Taylor expansion as $\varphi(r) = \varphi_0(r_0) + (r-r_0)\,\varphi_1(r_0) + (r-r_0)^2\,\varphi_2(r_0)$. As a feature in the object is moved from point to point, variations in φ_2 lead to the needed change in the illumination conditions. In our experiments using a pair of MLLs, we find that the inherent low-order wavefront errors, as well as higher-frequency errors due to sub-ångström variations in lens layer thicknesses [33], adequately provide the necessary diversity in the illumination beam without generating zeros in the far-field reference, and no additional diffuser is needed. Finally, the fact that near-field ptychography records holograms rather than far-field diffraction patterns means that the lateral object positions in the scan are evident in the holograms themselves, providing a way to determine the errors due to incorrect stage motion.

Here, we evaluate the performance of high-resolution imaging via near-field ptychography using high-NA MLLs by quantifying the resolution of a Siemens star test object and of a hierarchical nanoporous gold structure, demonstrating that imaging over large fields of view is reasonable and efficient. Results of a numerical study are then presented and used to compare this scheme to ptychography with a low-NA probe where the high-resolution information is recorded as "dark-field" scattering beyond the angular extent of the reference beam.

2. Experiments and results

A schematic diagram of our projection imaging experiment is shown in Fig. 1(b), which was carried out at the P11 beamline of the PETRA III (DESY, Hamburg) synchrotron radiation facility. A monochromatised and collimated beam with a photon energy of 17.4 keV (0.071 nm wavelength) was focused using a pair of MLLs. The lenses, each consisting of 10,854 bi-layers of SiC and WC, were fabricated in our laboratory by masked-layer deposition using magnetron sputtering onto flat silicon substrates [14,15]. At 17.4 keV they had focal lengths of 1.15 mm (horizontally focusing) and 1.25 mm (vertically focusing) and were positioned to focus to a common plane, as determined by speckle tracking [34] to a precision of about 200 nm which is lower than the depth of focus of the lenses. The NA of both lenses at this photon energy was 0.014. A pixel-array detector (Eiger, Dectris) with square pixels of width 75 µm was placed $L = 2.37$ m downstream of the focus. The flux in the focused beam, as measured by this detector, was 3.85×10^8 photons/s. Samples were placed downstream of the focus and were raster scanned in the transverse plane to obtain a dataset for near-field ptychography at a particular defocus distance Δf. The experimental parameters are listed in Table 1.

Table 1. Parameters used in the experiments and simulations

	Experiment (Siemens star)	Experiment (NPG)	High-NA simulation	Low-NA simulation
Wavelength (nm)	0.071	0.071	0.071	0.071
Aperture of lens (µm)	35	35	40	40
Focal length (mm)	1.2	1.2	1.43	143
NA of lens	0.014	0.014	0.014	0.00014
Defocus distance (µm)	200	73	37	10
Detector distance (m)	2.37	2.37	1.2	1.2
Magnification	11,850	32,465	32,432	/
Scan step size (nm)	300 (H) × 300(V)	250(H) × 100(V)	110	44
Scan points	441	63	50	500

We refer to the measurement without a sample as the reference beam, white field, or map of the lens pupil. This reference beam covered an area of 900 × 900 pixels on the detector and raw holograms were cropped to 1000 × 1000 pixels. The MLLs, as all diffractive optics, are chromatic, with a focal length that is inversely proportional to the wavelength. A change in wavelength thus changes the focus to object distance and so too the magnification. This must not change the extent of the full hologram by more than about half the width of a pixel, limiting the tolerable relative bandwidth to the inverse of the number of pixels across the beam at the detector. The relative bandwidth of 1.3×10^{-4} produced by the monochromator was indeed smaller than this.

2.1. Resolution estimation using a test object

We first characterized the high-NA near-field ptychography performance by using a Siemens star test object made of 750-nm thick gold on a silicon nitride membrane. The object was placed at a defocus distance Δf of 200 µm, where the beam width was 5.6 µm, giving a magnification of 11,850 corresponding to a 6.3 nm pixel size in the object space. A ptychographic dataset of 21 × 21 points was obtained with a step size of 0.3 µm in each direction, giving an overlap of 94.6% between neighboring holograms and an overall field of view of approximately 11.6 µm.

The exposure time per step was 1 s, giving 497 photons per pixel per frame within the lens pupil at the detector and a maximum scan-accumulated exposure of the object of 4470 photons/nm^2 in the central region of the scan (width 630 nm). One of the recorded projection holograms, uncorrected for the reference beam intensity, is shown in Fig. 1(b).

Prior to reconstruction, bad pixels of the detector were masked out. We adapted the open-source software package PyNX for the recovery of the complex-valued image of the object transmission and the lens wavefront. Starting from random initial guesses for both the probe wavefront and object transmission, a combination of different iterative phase retrieval algorithms was used: 1500 iterations of difference map (DM) [35], 2000 iterations of alternating projections (AP) [36], followed by 500 iterations of maximum likelihood gradient descent (ML) [37,38]. During reconstruction, we often observed a phase vortex appearing in the reconstructed probe, similar to vortices in reconstructed objects reported by others [39]. Such reconstructions were discarded. The equal-spaced raster scan can introduce periodic artefacts in the reconstructed image. To reduce these, we performed a smoothing of the object with a gaussian kernel during the DM and AP iterations and carried out the final ML iterations without smoothing. During iterative reconstruction, the diffracted field at the detector plane is calculated from the current estimates of the probe and the object, and then updated by the measured intensity. The pixels in the detector gap are not updated and are said to be floating. This process retrieves a pupil function that is consistent with the data. The results are shown in Fig. 2, including the 5.6-μm wide incident

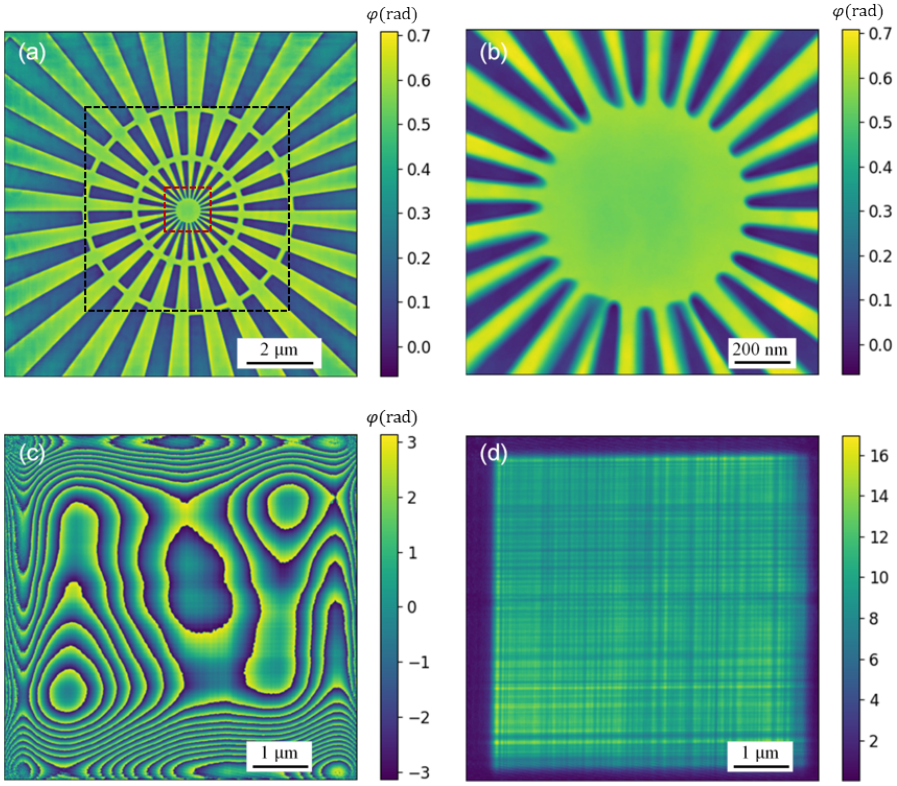

Fig. 2. Reconstruction results. (a) Phase image of the Siemens star transmission, obtained with a pixel size of 6.3 nm in both directions. Dashed black rectangle denotes the range of the steps of the scan. (b) Enlargement of the red-rectangle bounded central region of (a). (c) Phase and (d) normalized amplitude of the lens wavefront at the plane of the sample, covering 5.6 × 5.6 μm^2.

wavefront at the sample plane in Figs. 2(c) and 2(d). Although this wavefront aberration spans many waves, resulting in a point spread function at the focal plane [15] that is wider than the diffraction-limited spot size (equal to λ/NA = 5.1 nm), this does not hamper the image resolution obtained.

The innermost spokes of the Siemens star object can clearly be resolved in Figs. 2(a) and (b): evidently, the resolution is much better than the smallest spoke width of 50 nm and may be limited only by the Nyquist frequency (twice the pixel size, i.e., 12.6 nm). To obtain quantitative estimates of the resolution, we computed it via three different criteria: the edge criterion, which is a measure of the edge width [40]; the Fourier ring correlation (FRC) [41]; and the phase retrieval transfer function (PRTF) [42,43]. Figure 3 shows the edge profiles of spokes between the two rings from the phase image of the Siemens star shown in Fig. 2(a) along four different directions: vertical, horizontal and two orthogonal directions at 45° to the horizontal. The widths listed in the figure were determined by the distance between points corresponding to 25% and 75% of the total step height of the fitted error function (erf). The edge widths in the four directions are different. This is not necessarily an indication of anisotropic resolution. Instead, it is because the sample orientation was not corrected for the tilt of the chief ray of the focused beam relative to the optical axis and the 750-nm tall walls of the structure were therefore inclined to the focused beam by different angles. The chief ray is tilted in the diagonally direction by an angle of 1.8° since each MLL is an off-axis lens (such as shown in Fig. 1 in [34]) with the center of each lens deflecting the beam by 1.3°. Edges parallel to the plane of the combined beam tilt are sharp in the image, whereas perpendicular edges are broader, where the walls are no longer parallel to the beam. The average edge width in the four directions was 12.6 nm. The sharpest width was 7.1 nm, from edges parallel to the beam tilt, giving the best estimate of the resolution.

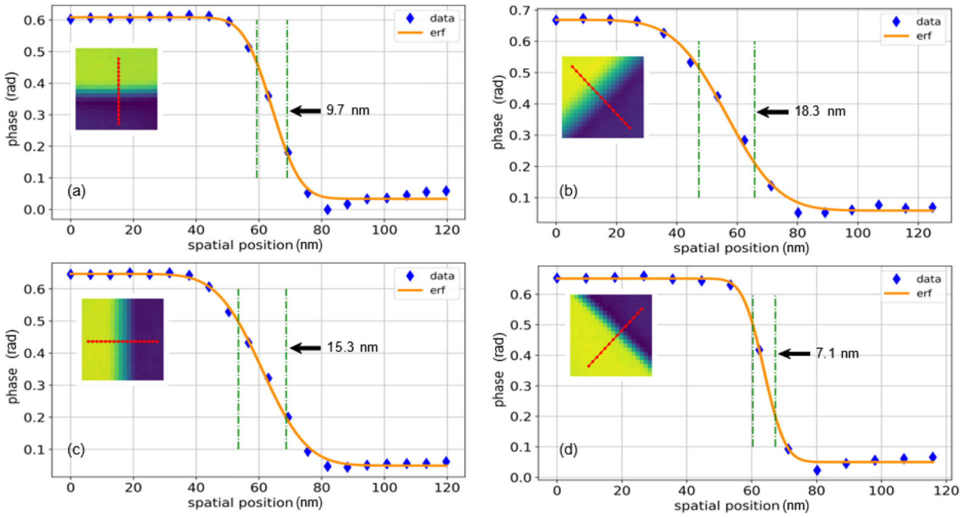

Fig. 3. Edge profiles of spokes in the phase image of the Siemens star object along vertical direction (a); horizontal direction (c) and two 45°-degree diagonal directions (b) and (d). The edge width is estimated from the distance between points corresponding to 25% and 75% of the total step height of the fitted error function. The resolution is estimated from the 7.1 nm width of the edge whose side-walls are oriented parallel to the chief ray of the focused beam.

To calculate the FRC, we first split the full dataset into two half-datasets by selecting every other frame of the full dataset. With these two half-datasets, each with double the step size in the fast-scan (vertical) direction, we obtained two independent reconstruction results, *A* and *B*, each with an average incident fluence of 1200 photons/nm^2. We smoothed the edges of each image and computed the FRC as [41]

$$\mathrm{FRC_{half}}(q) = \frac{\sum F_A(q) F_B^*(q)}{\sqrt{\sum |F_A(q)|^2 \sum |F_B(q)|^2}} \tag{1}$$

where $F_A(q)$ and $F_B(q)$ are the Fourier transforms of these two images as a function of the spatial frequency $q = (\sin\theta)/\lambda$ and * denotes the complex conjugate. Perfect imaging would give unity correlation over the full spatial frequency range. In practice, the FRC decreases with increasing q because high spatial frequency components generally have a lower power and are thus more easily affected by noise than low spatial frequency components [11]. Figure 4(a) shows a plot of $\mathrm{FRC_{half}}$ in green, giving a half-period resolution of 9.2 nm by the half-bit criterion [41]. However, we noticed that the images reconstructed from the full dataset appear to have better resolution than either of those from the half datasets. Even though two independent full datasets are unavailable, the FRC of the full dataset (with an average fluence of 2400 photons/nm^2) can be estimated from the so-called "CC-star" formula [44] as

$$\mathrm{FRC_{full}} = \sqrt{\frac{2\mathrm{FRC_{half}}}{1 + \mathrm{FRC_{half}}}}. \tag{2}$$

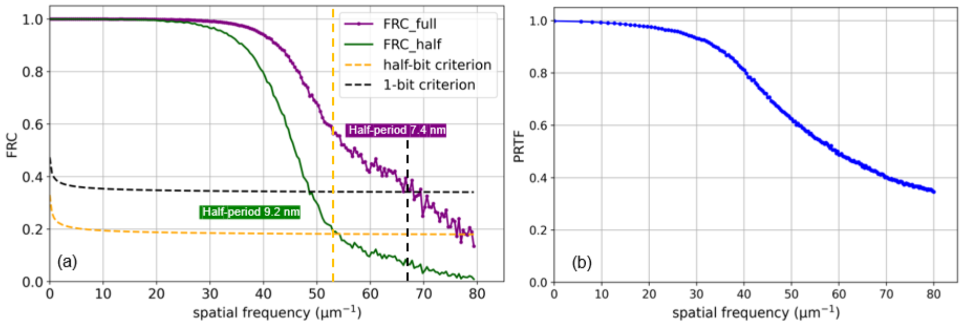

Fig. 4. Resolution evaluation of the reconstructed Siemens star object by (a) Fourier ring correlation, and (b) phase retrieval transfer function.

In this case, however, we must use the 1-bit threshold to quantify the resolution since this FRC metric estimates the correlation with the (unknown) true data without noise [44]. This metric, plotted in purple in Fig. 4(a), indicates a half-period resolution of 7.4 nm, a value that is consistent with the edge criterion estimation. Finally, we used a modified version of the PRTF to evaluate the stability of the iterative phase retrieval process, which is defined as follows:

$$\mathrm{PRTF}(q) = |\langle \exp[i\varphi(q)] \rangle| = \left| \left\langle \frac{G(q)}{|G(q)|} \right\rangle \right|, \tag{3}$$

where $G(q)$ is the Fourier transform of the reconstructed phase image and $\langle \ldots \rangle$ represents the average over a large number of independent reconstructions. If the Fourier phases fluctuate, the PRTF tends to zero, and if they are stable, the PRTF tends to one. Figure 4(b) shows the radial average of the PRTF obtained from 18 independent reconstructions. Even at the highest spatial frequency of 80 μm^{-1}, the PRTF value is approximately 0.4, indicating a stable phase retrieval process over the entire frequency range of the phase image. Together, the three resolution criteria are consistent with a half-period resolution that is not appreciably worse than the Nyquist sampling obtained with the particular choice of magnification of 11,850 (giving an image pixel width of 6.3 nm).

2.2. Imaging of nanoporous gold

Next, we imaged a nanoporous gold (NPG) sample with a hierarchical porous structure that confers high specific strength and low density [45]. The finest pores had a width of approximately 10 nm. A 1-µm wide column of this material was created by focused ion-beam milling—an SEM image of the object is shown in Fig. 5(a). A near-field ptychographic dataset was recorded at an even higher magnification factor than the Siemens star object (32,470 obtained at a defocus distance of 73 µm), giving a sampling size of 2.3 nm in the object space over a hologram width of 2.0 µm. The ptychographic dataset was acquired by stepping the object in a grid consisting of 3 × 21 locations (horizontal × vertical) with step sizes of 0.25 µm and 0.1 µm in the horizontal and vertical directions, and recording holograms with an exposure time of 5 s at each position, giving 2240 photons per pixel per frame within the lens pupil at the detector and a highest scan-accumulated exposure of 26,800 photons/nm^2 at the object plane. The reconstruction of the complex-valued transmission image of the NPG sample was carried out using the same procedure as for the Siemens star, as described in Sec. 2.1. Since this sample had a more complex structure than the Siemens star, reliable reconstructions were more readily obtained by using the probe function recovered from the Siemens star dataset as the initial probe—iterations with a random initial probe often converged slowly or even did not converge. The transmission image was still initialized from random values and reconstructed by running 2000 iterations of AP and then 500 iterations of ML.

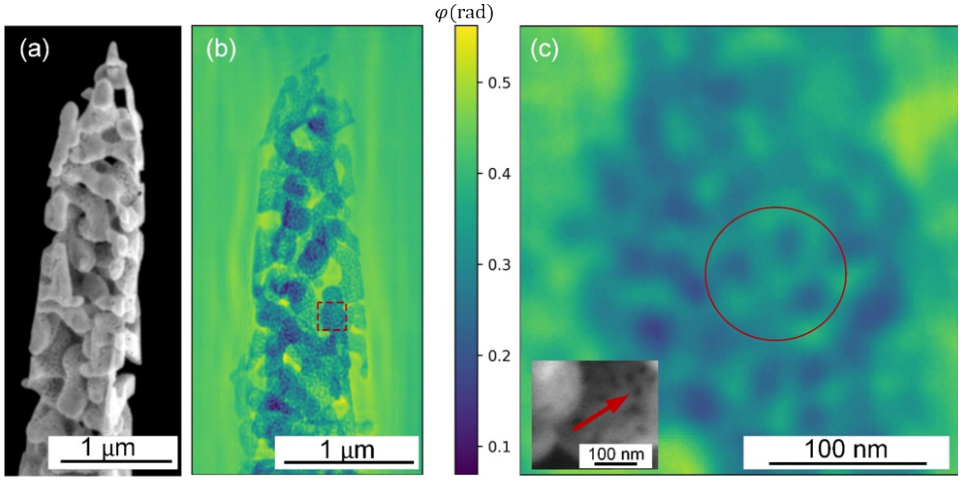

Fig. 5. Images of the NPG object: (a) An SEM image, and (b) the phase of the reconstructed X-ray image. (c) Enlargement of the dashed-line rectangle highlighted in (b). The inset indicates a region in the SEM image that shows holes in the nanoporous gold with a similar appearance to those in the circled area in the X-ray phase image. The colorbar pertains to both (b) and (c).

The recovered phase image of the NPG object is shown in Fig. 5(b). The small pores in the structure are well resolved across the entire field of view. An enlarged view of the image is given in Fig. 5(c), which can be compared with the similar region of the object as imaged by SEM (see the insert). Note that the X-ray image is a projection, whereas the SEM image shows only the surface details. These two images probably have different orientations and can not be exactly compared.

Employing the same resolution metrics as for the Siemens star object, the edge profiles along the horizonal and vertical directions of the edges of a pore are shown in Fig. 6. Although the images of the pore structures are not as high contrast as the bars of the Siemens star, the edge profiles indicate an edge width of approximately 8 nm. FRC curves calculated from two datasets (Eqn. (1)) and as estimated for the full dataset (Eqn. (2)) are shown in Fig. 7(a) in green and purple, respectively, with an average incident fluence of 10,100 photons/nm^2 for the half datasets. The latter indicates a half-period resolution of 5.4 nm by using 1-bit criterion, which is comparable with the 8 nm edge width. Figure 7(b) shows the phase-image PRTF curve, which remains above 0.6, indicating high stability of the reconstruction.

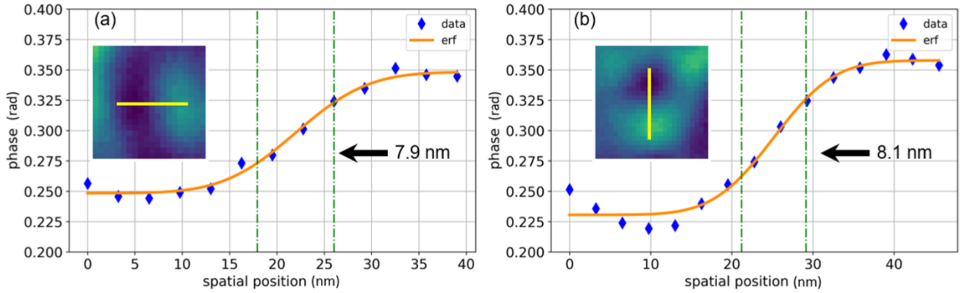

Fig. 6. Edge profiles of two pores from the reconstructed NPG along (a) horizontal and (b) vertical directions

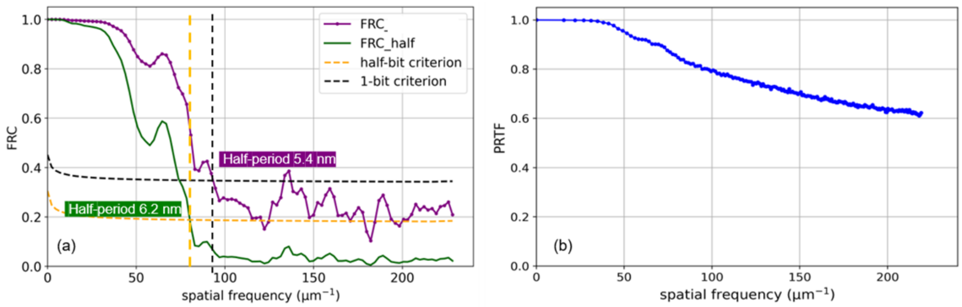

Fig. 7. Resolution evaluation of the reconstructed NPG image by (a) Fourier ring correlation, and (b) phase retrieval transfer function.

The resolution of the reconstructed image is slightly worse than the 5.1 nm diffraction-limited resolution of the lens pair, which ultimately limits the spatial frequency content captured in the dataset. Compared with the Siemens star dataset, yielding an image resolution of about 7 nm, the higher magnification of the NPG dataset gave a pixel size of 2.3 nm that matched the information capacity of the holograms. This comparison suggests that the resolution of the Siemens star image may be limited by the lower magnification. A possible reason why the evaluated resolution of the image of the NPG object was slightly worse than the diffraction limit is that the NPG object is three-dimensional with a thickness comparable to the depth of focus. For a coherent image (spatial frequencies recorded on the Ewald sphere), the depth of focus can be quantified as $\lambda/\mathrm{NA}^2 = 360$ nm, compared with the 1 μm thickness of the object. Other potential reasons for the worse resolution than expected may be experimental issues like stage vibrations or beam instabilities.

3. Numerical study and discussion

As mentioned in the Introduction, the projection holographic imaging modality using a high-NA illumination optics, as shown in Fig. 1(b), may have several advantages over the conventional diffraction-based imaging depicted in Fig. 1(c) and which can be characterized as ptychography with a low-NA lens. Although it was not feasible for us to carry out such conventional low-NA ptychography under similar conditions with the same sample, some published results suggest that high resolution requires additional care. At the PETRA III P06 beamline, for example, to avoid background scattering contamination from air, optics and apertures, the hard X-ray ptychographic microscope PtyNAMi [46] performs measurements in vacuum to achieve high resolution. In the soft X-ray spectrum, background scattering has also been seen to lower the imaging contrast and, therefore, the resolution [9].

To further compare these imaging modalities, we carried out a numerical study of ptychographic imaging with high-NA and low-NA reference beams. Similar comparisons of simulated experiments have been performed previously, including the comparison of holography with coherent diffractive imaging [47] and near-field ptychography with far-field ptychography [25]. These studies differed somewhat in their conclusions, but neither compared the performance of ptychographic imaging using a high-NA reference to that using a low-NA probe. Our near-field ptychographic setup differs from that considered by Du et al. (Ref. [25]), who simulated the incident illumination as unity magnitude and random phases. This does correspond to a divergent reference wave of a high NA (perhaps unfeasibly high, depending on the real-space pixel size used in the simulation) but with an intensity distribution in the far field that follows a negative binomial distribution where the most common value is zero [48]. That would require measurements of a high dynamic range and would not boost the signal as uniformly as the divergent beam from a lens, which might explain their finding that near-field ptychography performed slightly worse.

We simulated the datasets using a digital picture of a nanoporous gold slab as our object, obtained from an SEM acquisition and converted into a pure phase object with a phase ranging from -0.25 to 0.25 radians and a pixel size of 2.2 nm. A small subregion of the ground-truth object is shown in Fig. 8(a) and is used as the region of interest. It includes high-frequency components that have the appearance of noise. The parameters of the simulated optical systems are given in Table 1. The high-NA illumination lens was the same as in the experiment, but the focal length of the low-NA illumination lens was set to be one hundred times larger, giving an NA of 0.00014. As in the experiment, the lens apertures were taken to be square. The aberrations of the lenses were also set to be the same as those in the experiment, with an RMS (root mean square) wavefront error of 2.16 waves. The detector, with a 75 µm pixel width and 512×512 pixels, was set to a distance of 1.2 m in both cases, giving a scattering angle at the center edge of 0.016 radians to record a maximum spatial frequency of 225 μm^{-1} or a half-period resolution of 2.2 nm. The defocus was set to 37 µm for the high-NA case, where the beam size was 1.04 µm, and 10 µm for the low-NA case, which was within the depth of focus. The beam size for the low-NA case was 0.51 µm and the simulation was carried out close to focus to ensure we compare with the situation where the high-resolution information recorded on the detector was predominantly contained outside the lens pupil. For the high-NA case, this defocus gives a magnification of 32,432. The demagnified detector pixel size of 2.3 nm in that case is commensurate with the 2.2 nm sampling of the diffraction. The high-NA ptychographic data was simulated using the Fresnel scaling theorem [49] to avoid the need for large computation array sizes, and the diffraction patterns in the low NA case were simulated via Fourier-transform based Fresnel diffraction [50]. A spiral scan pattern was used to avoid raster-grid artifacts, with a step size of approximately 110 nm in the high-NA case and 44 nm in the low-NA case, giving a comparable overlap of approximately 90%. A similar field of view was covered in both scans, requiring fewer steps for the high-NA case (50 for high-NA versus 500 for low-NA).

To compare the imaging performance in terms of resolution, sensitivity to noise and background scattering, and dose efficiency, we simulated datasets with different scan-accumulated fluences (see Appendix A for details). We considered the ideal case of Poisson noise only (due to photon counting statistics) as well as Poisson noise plus a Gaussian-distributed background of 0.5% of

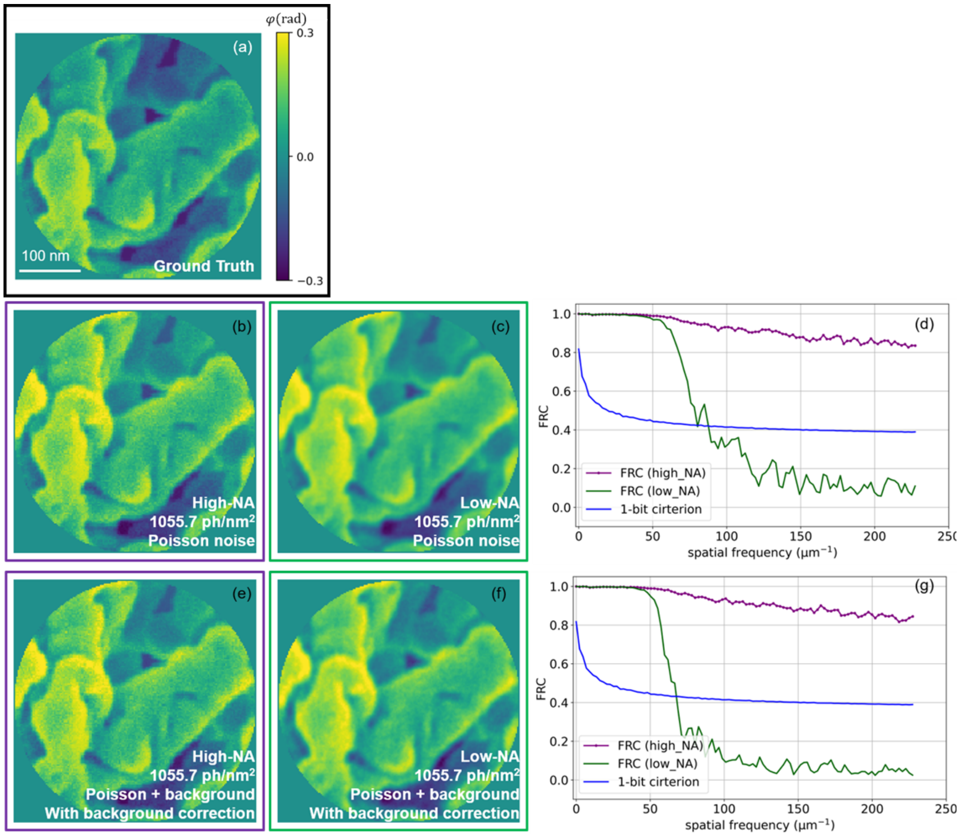

Fig. 8. Reconstruction results and FRC curves under different noise levels with incident fluence of 1055.7 photons/nm^2. (a) Ground truth of the simulated pure-phase object. (b) and (e) show the reconstructions in the high-NA case. (c) and (f) show the reconstructions in low-NA case. (d) and (g) show the FRC curves corresponding to the reconstructions shown in the same row. All images are shown on the same color scale ranging from −0.3 to 0.3 radian. Photons/nm^2 is represented by ph/nm^2.

the signal power. Such background is typically caused by scattering from MLL optics and various apertures, scattering from air, and incoherent scattering, such as fluorescence and Compton scattering. We modeled the background to have a uniform angular distribution across the detector based on measurements made at various detector distances. Detector readout noise or detector nonlinearities were not considered.

In both the high-NA and low-NA cases, we simulated two datasets, one with only Poisson noise and the other with Poisson noise plus background. For each of these datasets, we obtained three reconstructions starting from random independent initializations. During the iterative phase retrieval reconstruction (2000 iterations of AP and 200 iterations of ML), background correction [36] was used for the dataset with background. We calculated the FRC of each reconstruction against the ground truth and thus used the 1-bit threshold to estimate the resolution. Finally, we computed the average image of each set of three reconstructions and the average of their FRCs. In Fig. 8, we show the reconstruction results for an incident fluence of 1055.7 photons/nm^2.

The phase images and metrics shown in Figs. 8(b)-(g) for the high-NA and low-NA probes at a fixed fluence (and hence fixed dose) indeed show the advantages of using the high-NA reference, especially in the presence of background noise. The high-NA configuration results in a better resolution no matter whether there is background noise. Whereas, the resolution obtained in the low-NA case degrades with the addition of background, as apparent from the FRC plots and reconstructed images. The low-NA images in Fig. 8(c) and (f) appear somewhat smoother than their high-NA counterparts, but a comparison with the ground truth shows that the high-frequency details have a reduced contrast in the low-NA images.

Further reducing the fluence from 1055.7 photons/nm^2 has a greater effect on the high-NA case than on the low-NA case, as evident from the plot of the resolution of the reconstructed images as a function of the simulated fluence in Fig. 9. The reconstructions for this plot were computed via the same procedure as above, and the resolution (in units of the Nyquist spatial frequency of 225 µm^{-1}) was quantified from FRC curves using the 1-bit criterion. At the lowest fluence of 31.7 photons/nm^2, the low-NA case outperformed the high-NA case. At this fluence, there were only 2.5 photons per pixel on average recorded on the detector in the high-NA case. The high-NA reference beam causes a nearly even distribution of photons across the detector, whereas in the low-NA case the photons are concentrated at low scattering angles and thus into fewer pixels, making the signal-to-noise ratio higher. We find for this particular object and defocus setting that the resolution is roughly equal at a fluence of about 180 photons/nm^2 for the two cases when there is only Poisson noise, where the high-NA hologram has a signal of approximately 15 photons per pixel. At higher fluences, we see that the images using the high-NA lens improve in resolution and quality much faster than the low-NA case (see Appendix B for reconstructed images). Even though the SNR does improve with increasing fluence in the low-NA case, given the rapid decrease in the diffraction signal with scattering angle, this improvement occurs mainly at low resolution. When background scattering is considered, there is a significant deterioration in the resolution in the low-NA case. In contrast, there is almost no impact of background scattering on resolution for the high-NA case, which again illustrates its tolerance to this contamination.

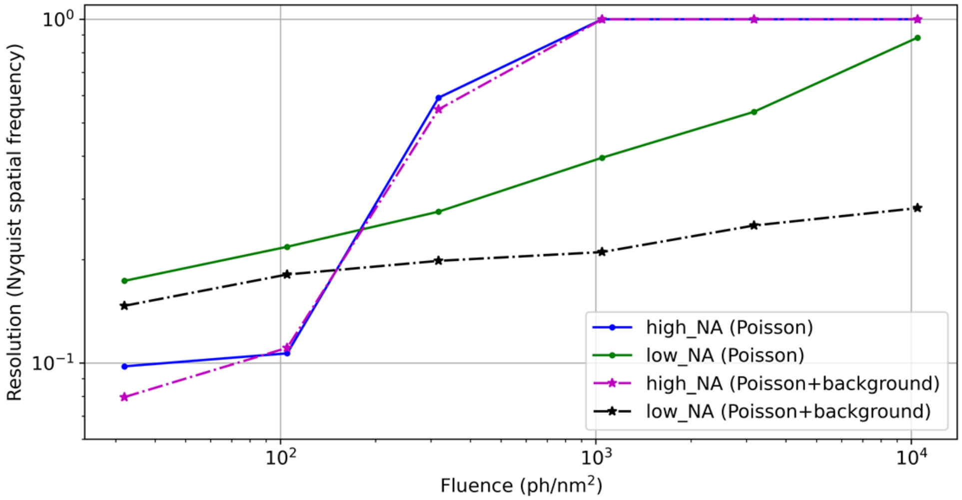

Fig. 9. Resolution of reconstructed images in both the high-NA and low-NA cases, as determined by the 1-bit criterion, for fluences of 31.7, 105.6, 316.7, 1055.7 (the case of Fig. 8), 3167.1, and 10557 photons/nm^2. Photons/nm^2 is represented by ph/nm^2.

Note that the experimental diffraction data from the nanoporous gold object were recorded at 2240 photons/pixel per frame and a maximum fluence of 26,800 photons/nm^2, but the resolution was not as good as that achieved by these simulations. This could be due to several reasons. The simulation considered a 2D object, but the nanoporous gold in the experiment was a 3D object. Since the thickness was not taken into account, this might have had an effect on the imaging resolution. In the experimental data, diffraction is not recorded in the gaps between detector panels, resulting in missing data.

4. Conclusion

We have demonstrated hard X-ray imaging at a sub-10 nm resolution by near-field ptychography using multilayer Laue lenses. This result was demonstrated on a hierarchical nanoporous gold object, which contains a network of pores with size of about 10 nm in diameter. We find that high-magnification point-projection imaging, phased within the framework of near-field ptychography, provides an easy way to obtain images—no special precautions were taken to reduce background scattering sources. The measurements are equivalent to near-field holograms and to defocused images obtained via a microscope with coherent illumination. The reference wave diverging from the lens focus interferes with the diffraction from the object and boosts this scattering signal by a large factor. While this boost also amplifies the effect of photon counting noise and hence does not necessarily improve the signal-to-noise ratio of the measurement, it does place the signal on a large bias that renders it insensitive to background scattering and avoids the need for measurements of a high dynamic range. This requires a sufficiently large divergence of the reference wave, which is achieved by our multilayer Laue lens system with a numerical aperture of NA = 0.014, giving a diffraction-limited resolution of 5 nm. The lenses are not perfect and exhibit both low-order wavefront aberrations and variations in the intensity across the wavefront. These have the effect of distorting and modulating the projection holograms. But, far from degrading the images, these defects provide the diversity needed for ptychographic phase retrieval. Another benefit of using lenses in near-field ptychography is that, unlike scattering from an object such as a pinhole or from a random diffuser, there are no zeros in the reference wave in the far field, so all spatial frequencies of the object are transferred more or less equally. Furthermore, and common to our previous work on imaging via speckle tracking [51], projection images are recorded directly on pixel-array detectors to avoid dose inefficiencies in optical imaging of a scintillator [23]. Through numerical simulations, we compared the performance of near-field ptychography using aberrated high-NA lenses against far-field ptychography with a focused probe of a much lower numerical aperture. In this case, the high-resolution information is recorded as a dark-field signal and is more susceptible to background scattering, as compared with the high-NA case, at least for exposures greater than 180 photons/nm^2. A large probe size in near-field ptychography requires far fewer steps for obtaining a given field of view, enabling high-speed imaging when detector readout and stage motion are limiting factors. Near-field ptychography with high-NA optics may thus provide an optimal way for imaging at the highest resolutions and speeds at current and upcoming synchrotron radiation facilities for materials studies.

Appendix A. Incident fluence calculation

The integrated fluence distribution over the course of a scan is the convolution of the beam intensity profile at the sample plane with the scan positions. When the beam size is much larger than the step size, as it is in near-field ptychography, the fluence that the sample experiences (and hence also the dose) is maximum at the center of the scan area. The normalized fluence distributions for the calculated datasets are shown in Fig. 10, without background noise, and indicating the central region where the maximum average fluence was calculated. This was also the region used for the determination of the FRC. The simulated scans followed spiral paths. For the low-NA case, there were 500 scan points with a scan step of 44 nm, and 50 scan points with a step size of 110 nm for the high-NA case.

The simulated datasets for different fluences were obtained by setting the total photon number in the probe, per frame. In the low-NA case, these were 6.15×10^4, 2.05×10^5, 6.15×10^5, 2.05×10^6, 6.15×10^6, and 2.05×10^7, giving maximum average fluences of 31.7 105.6, 316.7,

Optics EXPRESS

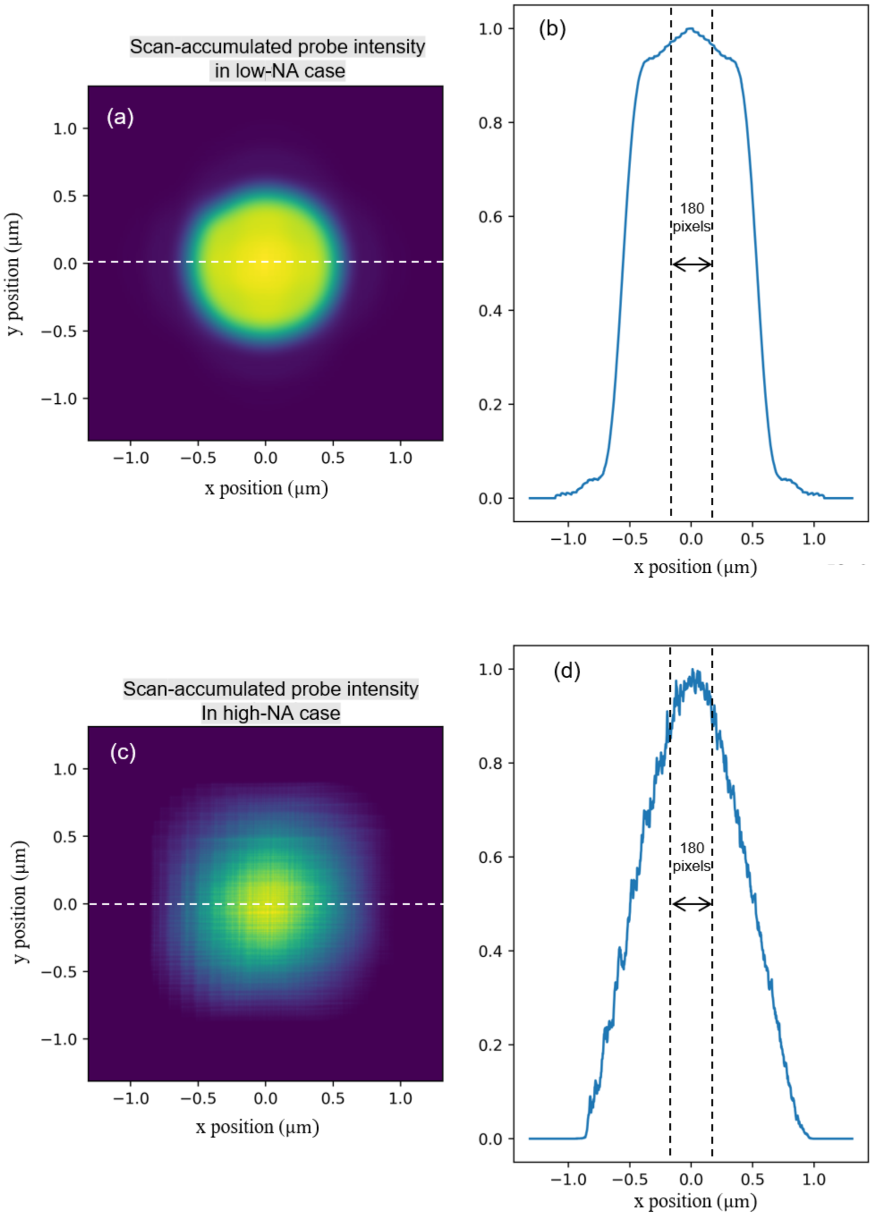

Scan-accumulated probe intensity in low-NA case

Scan-accumulated probe intensity In high-NA case

Fig. 10. Scan-accumulated normalized incident intensity distributions for the simulated datasets, and plots of these along the dashed white lines for (a),(b) low-NA case, and (c),(d) the high-NA case. The region of interest is denoted by the “180 pixels” in (b) and (d).

1055.7, 3167.1, and 10557 photons/nm^2, respectively. In the high-NA case, the photon number per frame was increased to give the same maximum average fluences. These values were 6.45×10^5, 2.15×10^6, 6.45×10^6, 2.15×10^7, 6.45×10^7, and 2.15×10^8.

Appendix B. Reconstructed phase images and corresponding FRC curves in the numerical study

To investigate whether background scattering can be mitigated, reconstructions were carried out both with and without background correction. Figure 8 only shows the results with background correction. Figure 11 displays the complete reconstruction results over a wider range of fluences, and Fig. 12 gives the corresponding FRC curves. From the comparison between reconstructions with and without background correction, it is evident that background correction does improve images obtained in the low-NA case, especially when fluence is higher than 3167.1 photons/nm^2; and has a minor effect on the high-NA case where the background noise hardly affects the high-NA imaging, presumably due to the strong reference wave, as shown in Fig. 11 and Fig. 12.

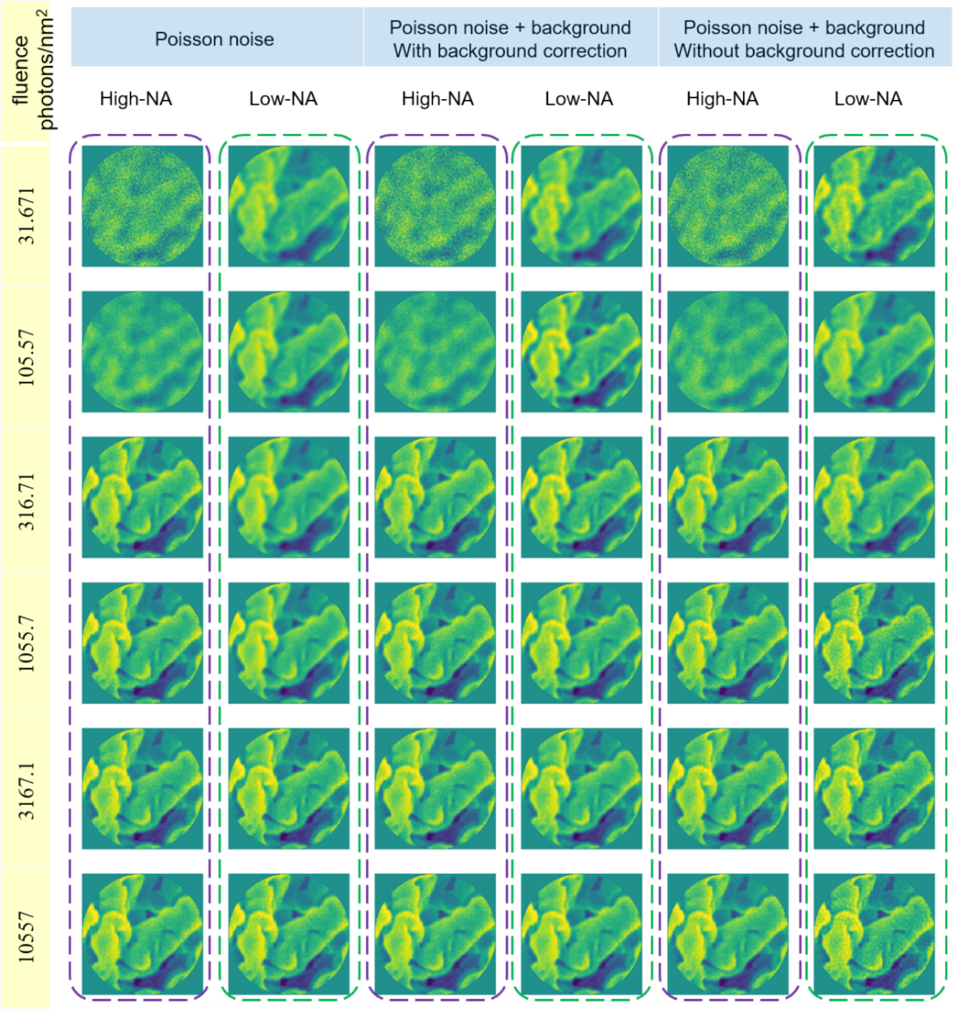

Fig. 11. Reconstructed phase images in both high-NA and low-NA cases under different fluence and noise/reconstruction conditions.

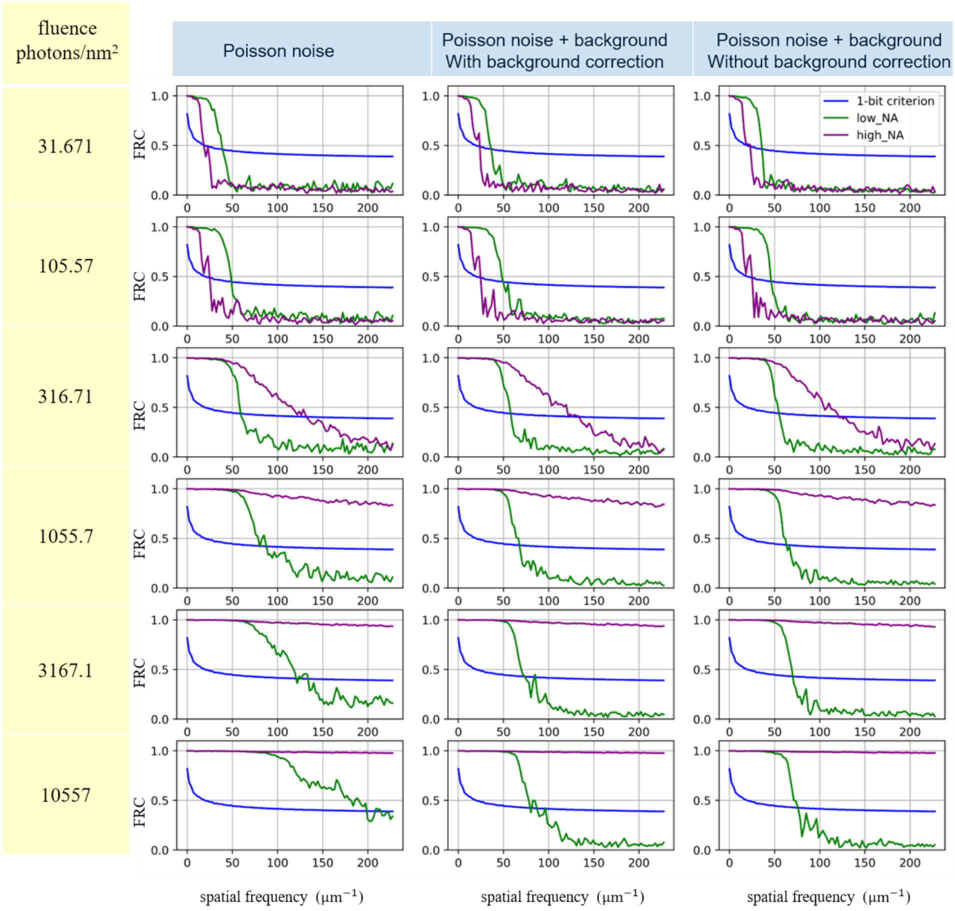

Fig. 12. FRC curves corresponding to the images in Fig. 11.

Funding. Deutsche Forschungsgemeinschaft (390715994, EXC 2056).

Acknowledgments. We acknowledge Sabrina Schneider, Harumi Nakatsutsumi, Tjark Delmas (DESY) and Martin Domarackу́ for their technical support and Johanna Hakanpää, Sofiane Saouane, and Guillaume Pompidor for assistance at beamline P11 of the PETRA III facility at DESY. We thank Patrick Huber (DESY and TUHH) for helpful suggestions. We acknowledge support from DESY (Hamburg, Germany), a member of the Helmholtz Association HGF. This research was supported in part by the Maxwell computational resources operated at DESY. Additional support was provided by the Cluster of Excellence CUI: Advanced Imaging of Matter of the Deutsche Forschungsgemeinschaft (DFG) – EXC 2056 – project ID 390715994.

Disclosures. The authors declare no conflicts of interest.

Data availability. Data underlying the results presented in this paper are not publicly available at this time but may be obtained from the authors upon reasonable request.

References

1. A. Michelson, B. Minevich, H. Emamy, *et al.*, "Three-dimensional visualization of nanoparticle lattices and multimaterial frameworks," Science **376**(6589), 203–207 (2022).
2. M. Holler, M. Odstrcil, M. Guizar-Sicairos, *et al.*, "Three-dimensional imaging of integrated circuits with macro-to nanoscale zoom," Nat. Electron. **2**(10), 464–470 (2019).
3. F. Pfeiffer, "X-ray ptychography," Nat. Photonics **12**(1), 9–17 (2018).
4. M. Dierolf, A. Menzel, P. Thibault, *et al.*, "Ptychographic X-ray computed tomography at the nanoscale," Nature **467**(7314), 436–439 (2010).
5. H. N. Chapman and K. A. Nugent, "Coherent lensless X-ray imaging," Nat. Photonics **4**(12), 833–839 (2010).

6. P. Thibault, M. Dierolf, A. Menzel, *et al.*, "High-Resolution Scanning X-ray Diffraction Microscopy," Science **321**(5887), 379–382 (2008).
7. M. Töpperwien, F. van der Meer, C. Stadelmann, *et al.*, "Three-dimensional virtual histology of human cerebellum by X-ray phase-contrast tomography," Proc. Natl. Acad. Sci. **115**(27), 6940–6945 (2018).
8. J. Miao, T. Ishikawa, I. K. Robinson, *et al.*, "Beyond crystallography: Diffractive imaging using coherent x-ray light sources," Science **348**(6234), 530–535 (2015).
9. D. A. Shapiro, Y.-S. Yu, T. Tyliszczak, *et al.*, "Chemical composition mapping with nanometre resolution by soft X-ray microscopy," Nat. Photonics **8**(10), 765–769 (2014).
10. M. Holler, A. Diaz, M. Guizar-Sicairos, *et al.*, "X-ray ptychographic computed tomography at 16 nm isotropic 3D resolution," Sci. Rep. **4**(1), 3857 (2014).
11. C. Jacobsen, *X-Ray Microscopy* (Cambridge University Press, 2019).
12. M. R. Howells, T. Beetz, H. N. Chapman, *et al.*, "An assessment of the resolution limitation due to radiation-damage in X-ray diffraction microscopy," J. Electron Spectros. Relat. Phenomena **170**(1-3), 4–12 (2009).
13. H. Yan, R. Conley, N. Bouet, *et al.*, "Hard x-ray nanofocusing by multilayer Laue lenses," J. Phys. D: Appl. Phys. **47**(26), 263001 (2014).
14. S. Bajt, M. Prasciolu, H. Fleckenstein, *et al.*, "X-ray focusing with efficient high-NA multilayer Laue lenses," Light: Sci. Appl. **7**(3), 17162 (2017).
15. J. L. Dresselhaus, H. Fleckenstein, M. Domaracký, *et al.*, "Precise wavefront characterization of x-ray optical elements using a laboratory source," Rev. Sci. Instrum. **93**(7), 073704 (2022).
16. F. Seiboth, A. Schropp, M. Scholz, *et al.*, "Perfect X-ray focusing via fitting corrective glasses to aberrated optics," Nat. Commun. **8**(1), 14623 (2017).
17. F. Seiboth, A. Kubec, A. Schropp, *et al.*, "Rapid aberration correction for diffractive X-ray optics by additive manufacturing," Opt. Express **30**(18), 31519–31529 (2022).
18. J. C. H. Spence, U. Weierstall, and M. Howells, "Coherence and sampling requirements for diffractive imaging," Ultramicroscopy **101**(2-4), 149–152 (2004).
19. M. Stockmar, P. Cloetens, I. Zanette, *et al.*, "Near-field ptychography: phase retrieval for inline holography using a structured illumination," Sci. Rep. **3**(1), 1927 (2013).
20. J. C. H. Spence, "STEM and shadow-imaging of biomolecules at 6 eV beam energy," Micron **28**(2), 101–116 (1997).
21. T. Latychevskaia, "Holography and Coherent Diffraction Imaging with Low-(30–250 eV) and High-(80–300 keV) Energy Electrons: History, Principles, and Recent Trends," Materials **13**(14), 3089 (2020).
22. J. A. Lin and J. M. Cowley, "Calibration of the operating parameters for an HB5 stem instrument," Ultramicroscopy **19**(1), 31–42 (1986).
23. J. C. H. H. Spence, W. Qian, and A. J. Melmed, "Experimental low-voltage point-projection microscopy and its possibilities," Ultramicroscopy **52**(3-4), 473–477 (1993).
24. P. Cloetens, W. Ludwig, J. Baruchel, *et al.*, "Holotomography: Quantitative phase tomography with micrometer resolution using hard synchrotron radiation x rays," Appl. Phys. Lett. **75**(19), 2912–2914 (1999).
25. M. Du, D. Gürsoy, and C. Jacobsen, "Near, far, wherever you are: Simulations on the dose efficiency of holographic and ptychographic coherent imaging," J. Appl. Crystallogr. **53**(3), 748–759 (2020).
26. R. Battistelli, D. Metternich, M. Schneider, *et al.*, "Coherent x-ray magnetic imaging with 5 nm resolution," Optica **11**(2), 234–237 (2023).
27. J. Hagemann and T. Salditt, "Coherence-resolution relationship in holographic and coherent diffractive imaging," Opt. Express **26**(1), 242–253 (2018).
28. T. Shintake, "Possibility of single biomolecule imaging with coherent amplification of weak scattering x-ray photons," Phys. Rev. E **78**(4), 041906 (2008).
29. S. Eisebitt, J. Lüning, W. F. Schlotter, *et al.*, "Lensless imaging of magnetic nanostructures by X-ray spectro-holography," Nature **432**(7019), 885–888 (2004).
30. W. F. Schlotter, J. Lüning, R. Rick, *et al.*, "Extended field of view soft x-ray Fourier transform holography: toward imaging ultrafast evolution in a single shot," Opt. Lett. **32**(21), 3110–3112 (2007).
31. M. R. Howells, C. J. Jacobsen, S. Marchesini, *et al.*, "Toward a practical X-ray Fourier holography at high resolution," Nucl. Instrum. Methods Phys. Res., Sect. A **467-468**, 864–867 (2001).
32. I. McNulty, J. Kirz, C. Jacobsen, *et al.*, "High-Resolution Imaging by Fourier Transform X-ray Holography," Science **256**(5059), 1009–1012 (1992).
33. K. T. Murray, A. F. Pedersen, I. Mohacsi, *et al.*, "Multilayer Laue lenses at high X-ray energies: performance and applications," Opt. Express **27**(5), 7120–7138 (2019).
34. N. Ivanov, J. Lukas Dresselhaus, J. Carnis, *et al.*, "Robust ptychographic X-ray speckle tracking with multilayer Laue lenses," Opt. Express **30**(14), 25450–25473 (2022).
35. V. Elser, I. Rankenburg, and P. Thibault, "Searching with iterated maps," Proc. Natl. Acad. Sci. **104**(2), 418–423 (2007).
36. S. Marchesini, A. Schirotzek, C. Yang, *et al.*, "Augmented projections for ptychographic imaging," Inverse Probl. **29**(11), 115009 (2013).
37. M. Odstrčil, A. Menzel, and M. Guizar-Sicairos, "Iterative least-squares solver for generalized maximum-likelihood ptychography," Opt. Express **26**(3), 3108–3123 (2018).

38. P. Thibault and M. Guizar-Sicairos, “Maximum-likelihood refinement for coherent diffractive imaging,” New J. Phys. **14**(6), 063004 (2012).
39. M. Stockmar, I. Zanette, M. Dierolf, *et al.*, “X-ray near-field ptychography for optically thick specimens,” Phys. Rev. Appl. **3**(1), 014005 (2015).
40. L. Reimer, “Scanning electron microscopy: physics of image formation and microanalysis,” Meas. Sci. Technol. **11**(12), 1826 (2000).
41. M. Van Heel and M. Schatz, “Fourier shell correlation threshold criteria,” J. Struct. Biol. **151**(3), 250–262 (2005).
42. L. J. Allen and M. P. Oxley, “Phase retrieval from series of images obtained by defocus variation,” Opt. Commun. **199**(1-4), 65–75 (2001).
43. H. N. Chapman, A. Barty, S. Marchesini, *et al.*, “High-resolution ab initio three-dimensional x-ray diffraction microscopy,” J. Opt. Soc. Am. A **23**(5), 1179–1200 (2006).
44. P. A. Karplus and K. Diederichs, “Linking crystallographic model and data quality,” Science **336**(6084), 1030–1033 (2012).
45. S. Shi, Y. Li, B.-N. Ngo-Dinh, *et al.*, “Scaling behavior of stiffness and strength of hierarchical network nanomaterials,” Science **371**(6533), 1026–1033 (2021).
46. A. Schropp, R. Döhrmann, S. Botta, *et al.*, “PtyNAMi: ptychographic nano-analytical microscope,” J. Appl. Crystallogr. **53**(4), 957–971 (2020).
47. J. Hagemann and T. Salditt, “The fluence–resolution relationship in holographic and coherent diffractive imaging,” J. Appl. Crystallogr. **50**(2), 531–538 (2017).
48. J. W. Goodman, *Speckle Phenomena in Optics: Theory and Applications* (Roberts and Company Publishers, 2007).
49. D. Paganin, *Coherent X-Ray Optics* (Oxford University Press on Demand, 2006).
50. W. Zhang, H. Zhang, C. Sheppard, *et al.*, “Analysis of numerical diffraction calculation methods: from the perspective of phase space optics and the sampling theorem,” J. Opt. Soc. Am. A **37**(11), 1748–1766 (2020).
51. A. J. Morgan, K. T. Murray, M. Prasciolu, *et al.*, “Ptychographic X-ray speckle tracking with multi-layer Laue lens systems,” J. Appl. Crystallogr. **53**(4), 927–936 (2020).